New limits to CO outgassing in Centaurs

Michał Drahus,[1]★ Bin Yang,[2,3] Dariusz C. Lis[4,5] and David Jewitt[6,7]

[1]*Astronomical Observatory, Jagiellonian University, ul. Orla 171, 30-244 Kraków, Poland*

[2]*European Southern Observatory, Alonso de Córdova 3107, Vitacura, Casilla 19001, Santiago de Chile, Chile*

[3]*Yunnan Astronomical Observatory, Chinese Academy of Sciences, P.O. Box 110, Kunming 650011, Yunnan, China*

[4]*LERMA, Observatoire de Paris, PSL Research University, CNRS, Sorbonne Universités, UPMC Univ. Paris 06,*

61 Avenue de l'Observatoire, 75014 Paris, France

[5]*Division of Physics, Mathematics and Astronomy, California Institute of Technology, 1200 E California Blvd, Pasadena, CA 91125, USA*

[6]*Department of Earth, Planetary and Space Sciences, University of California at Los Angeles, 595 Charles E Young Dr E, Los Angeles, CA 90095, USA*

[7]*Department of Physics and Astronomy, University of California at Los Angeles, 475 Portola Plaza, Los Angeles, CA 90095, USA*

ABSTRACT

Centaurs are small Solar system objects orbiting between Jupiter and Neptune. They are widely believed to be escapees from the trans-Neptunian region on their way to become Jupiter-family comets. Indeed, some Centaurs exhibit the characteristic cometary appearance. The sublimation of carbon monoxide has been proposed as a driver of activity in distant comets, but no strong detection of gaseous CO in a Centaur other than 29P/Schwassmann-Wachmann 1 has been reported to date. Here we report the results of a deep search for CO outgassing in three Centaurs: (315898), (342842), and (382004). Our survey was carried out using the Caltech Submillimeter Observatory on nine nights in late 2011. The targeted rotational line J(2–1) of CO is undetected in all three objects in spite of high instrumental sensitivity. We find the model-dependent 3σ upper limits to the CO production rate of 2.13×10^{27} molecules s^{-1} for (315898), 1.32×10^{27} molecules s^{-1} for (342842), and 1.17×10^{27} molecules s^{-1} for (382004), which are among the most sensitive obtained to date. These upper limits are consistently analysed in the context of published CO data of 14 Centaurs and one well-observed long-period comet, C/1995 O1 (Hale-Bopp), and support an earlier suggestion that the surfaces of most Centaurs are not dominated by exposed CO ice.

Key words: comets: general – Kuiper belt: general – minor planets, asteroids: individual: 315898 – minor planets, asteroids: individual: 342842 – planets, asteroids: individual: 382004 – radio lines: general.

1 INTRODUCTION

Centaurs are small Solar system objects belonging entirely to the giant-planet region. Strictly speaking, we adopt a definition similar to Jewitt (2009), and classify as Centaurs all minor bodies with perihelion distances greater than the semimajor axis of Jupiter and semimajor axes smaller than the semimajor axis of Neptune, excluding planetary satellites and Trojans. Historically, the first known object satisfying these criteria was comet 29P/Schwassmann-Wachmann 1, discovered in 1927, which follows a nearly circular orbit ∼0.8 au beyond the orbit of Jupiter. However, the existence of Centaurs as a population was not recognized until the early 1990s. In particular, in 1963 comet 39P/Oterma was ejected by Jupiter on to a new orbit spanning between the orbits of Jupiter and Saturn, and in this way became – from the

current perspective – the second known Centaur. Later, in 1977, Charles Kowal discovered the third member of this population, Chiron (Kowal & Gehrels 1977), with an orbit spanning approximately between the orbits of Saturn and Uranus. But the full significance of Centaurs was recognized only after the discovery of the Kuiper belt beyond the orbit of Neptune (Jewitt & Luu 1993, 1995), which all of a sudden made them fit into the 'bigger picture' as a transition population between the trans-Neptunian region and the domain of Jupiter-family comets (Levison & Duncan 1997). This coincided with an increase of their discovery rate, leading to the identification of 213 Centaurs as of UT 2016 March 1.

The population of Centaurs contains both objects displaying cometary activity, even at large heliocentric distances (up to the orbit of Uranus), as well as objects which appear inactive even at perihelia (down to the distance of Jupiter). For example, the first two known Centaurs, 29P and 39P, are comets, discovered thanks to the extra brightness from the coma. In fact, 29P has probably never been seen inactive (Jewitt 1990; Meech et al. 1993), but frequently

★ E-mail: drahus@oa.uj.edu.pl

observed to burst out at irregular time intervals and with a range of amplitudes (Trigo-Rodríguez et al. 2008, 2010). The third known Centaur, Chiron, was discovered with 'stellar appearance' (Kowal & Gehrels 1977) and classified as asteroid (2060), but later developed weak activity, which earned it the additional comet number 95P. The activity of Chiron was originally inferred from the rapid brightness increase in the late 1980s (Tholen, Hartmann & Cruikshank 1988), further supported by the decline of the rotational amplitude (Bus, Bowell & French 1988), and definitely confirmed by the direct detection of the coma (Meech & Belton 1989). Initially attributed to the then-upcoming perihelion passage in the early 1996, the activity of Chiron turned out to be episodic or quasi-periodic (e.g. Duffard et al. 2002, and references therein), with the most surprising result being perhaps that the brightness was eventually close to the minimum at perihelion but close to the maximum at the last aphelion. In this sense Chiron's activity resembles 29P, although the latter object varies over a considerably larger range and on a much shorter time-scale. According to the study by Jewitt (2009), about 13 per cent of the known Centaurs display cometary activity at a given time.

The sublimation of carbon monoxide (CO) has been proposed as a mechanism generating activity in distant comets originating from the Oort cloud (e.g. Biver et al. 1996; Jewitt, Senay & Matthews 1996). Gaseous CO was also robustly detected in 29P (Senay & Jewitt 1994) following an earlier detection of the CO^+ cation (Cochran, Barker & Cochran 1980; Larson 1980) produced in the object's coma by photoionization of the neutral CO. The CO outgassing rate is observed to vary between 2 and 8×10^{28} molec s^{-1} (Biver 1997), a surprisingly narrow range compared to the explosive behaviour seen in the optical, and poorly correlated with the latter (Biver 2001).

Owing to the non-negligible (albeit weak) permanent electric dipole moment (resulting from the asymmetric charge distribution) equal to 0.110 11 D (cf. CDMS;[1] Müller et al. 2005), the CO molecule generates measurable rotational emission lines. It also has a relatively small moment of inertia, which translates into a relatively large rotational constant of 57.635 968 GHz (cf. CDMS; Müller et al. 2005), thanks to which the lines can be observed from the ground in the millimetre and submillimetre atmospheric windows. Furthermore, at low rotational temperatures, characteristic of the cometary comae in the outer Solar system, the CO molecules are spread over only the first few rotational energy levels J in the ground electronic and vibrational states, producing a very narrow energy-level distribution (Crovisier 1993). Therefore, radio spectroscopy of the low-J rotational emission lines is an obvious first choice for the studies of CO in the comae of Centaurs. Indeed, the historical detection of the CO $J(2-1)$ line in 29P (Senay & Jewitt 1994) was followed up by a detection in the infrared only recently (Paganini et al. 2013) and will be even harder to achieve in the ultraviolet (cf. Crovisier 1993).

Whereas gaseous CO in 29P is routinely observed at millimeter wavelengths, no strong detection of CO (or any other molecular gas) in any other Centaur has been reported to date, although unconfirmed tentative detections of CN (Bus et al. 1991) and CO (Womack & Stern 1997) were reported for Chiron. This situation motivated several previous observational efforts (Rauer et al. 1997; Bockelée-Morvan et al. 2001; Jewitt, Garland & Aussel 2008) and was also the main inspiration for this work.

2 OBSERVATIONS

2.1 New observations and data reduction

In late 2011, we observed three Centaurs: 2008 QD$_4$ (315898), 2008 YB$_3$ (342842), and 2010 RM$_{64}$ (382004), searching for the $J(2-1)$ rotational transition of CO at $\nu_{ul} = 230.538\ 0000$ GHz (rest frequency). These three objects were discovered by the La Sagra, Siding Spring, and La Silla – QUEST (Rabinowitz et al. 2012) surveys, respectively. We used the 10.4 m Leighton Telescope of the Caltech Submillimeter Observatory (CSO) atop Mauna Kea (Hawaii), which has the full width at half-maximum (FWHM) beam size of 32.4 arcsec at the observed frequency. All three objects were visited nightly in a fixed order, starting from (382004) in a long block at the beginning of the night, followed by (315898) in a shorter block later in the night, and finishing with (342842) in another long block at the end of the night. The last two targets were observed on nine consecutive nights: (315898) between UT 2011 October 24.52 and November 1.56, and (342842) between UT 2011 October 24.59 and November 1.67. The first target, (382004), was missed on the last night due to fog at the beginning of that night and was observed on eight consecutive nights from UT 2011 October 24.32 to 31.46. The data were taken almost exclusively in very good weather conditions (Fig. 1) and we did not encounter any significant technical interruptions. In Table 1, we present the orbital and physical characteristics of these objects taken from the literature.

Topocentric positions of the Centaurs were continuously calculated by the telescope control system from the input geocentric ephemerides (interpolated in the real time), which we generated with the JPL *Horizons* system[2] (Giorgini et al. 1997). The ephemerides were accurate to ~1 arcsec for (382004), and <0.5 arcsec for (315898) and (342842). We consistently took data in the *beam-switching* mode, with the secondary mirror chopping in azimuth between the target and sky background, and the dish positioned between the two. We used 0.5678 Hz switching frequency and 3 arcmin separation angle ('throw'). On the first two nights, the data were taken using the older 230 GHz receiver mounted at the Nasmyth focus ('sidecab'), but later we switched to the wideband Z-Rex receiver (earlier unavailable for technical reasons) mounted at the bent Cassegrain focus. Both instruments are double-sideband single-polarization designs, but Z-Rex outperforms the older 230 GHz receiver in terms of the system temperature by approximately a factor of 2. As for the backend system, we used the 8192-channel fast Fourier transform spectrometer configured to produce 61 kHz spectral-channel spacing and 500 MHz of total bandwidth. The absolute frequency scale was automatically converted into the relative radial-velocity scale (through the classical Doppler law) corrected for the topocentric velocities of our targets continuously calculated from the input geocentric ephemerides (interpolated in the real time). Zero velocity corresponds to the transition rest frequency, negative velocities to higher frequencies (blueshift), and positive velocities to lower frequencies (redshift). At the transition frequency of CO $J(2-1)$, the channel width is 79.4 m s^{-1} ($R = 3.78 \times 10^6$), which is more than sufficient to resolve the line profile in practically any cosmic environment. The spectra were automatically calibrated in terms of the antenna temperature T'_A (i.e. corrected for atmospheric attenuation and the signal band gain) using the standard chopper-wheel technique (Ulich & Haas 1976; Kutner & Ulich

---

[1] The Cologne Database for Molecular Spectroscopy is available online at http://www.astro.uni-koeln.de/cdms.
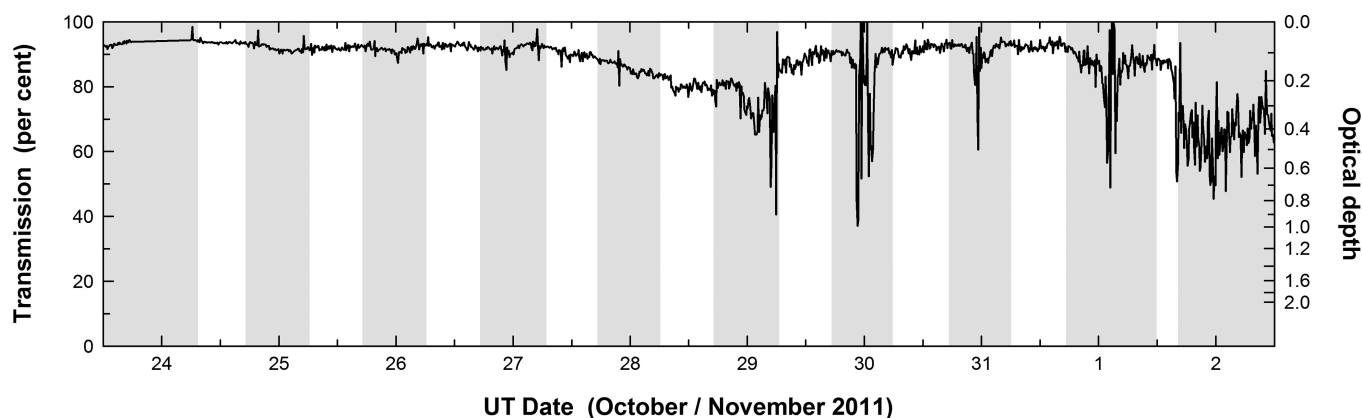
[2] http://ssd.jpl.nasa.gov/?horizons

Figure 1. Zenith atmospheric transmission during our run. The shaded windows indicate the periods in which data were not taken (generally daytime). The transmission is equal to $e^{-\tau(\nu)}$ and was calculated from the optical depth τ (indicated by the right axis) measured at $\nu = 225$ GHz at zenith by the CSO taumeter. Given that the taumeter frequency is very close to the observed frequency of CO, equal to 230.538 GHz, we adopt this transmission curve as representative of our data.

Table 1. Selected orbital and physical properties of our objects of interest.

Object	Perihelion[a] (UT Date)	P^b (yr)	q^c (au)	a^d (au)	Diameter (km)	Ref.[e]
(315898)	2010 Aug 28	24.504	5.442	8.436	22 ± 8	*
(342842)	2011 Mar 02	39.772	6.487	11.651	67 ± 1	[1]
(382004)	2012 Oct 17	87.598	6.157	19.724	21 ± 2	[1]
166P/NEAT	2002 May 21	51.728	8.564	13.883	15 ± 13	**
(60558) Echeclus	2015 Apr 22	35.062	5.816	10.712	65 ± 2	[2]
(55576) Amycus	2003 Jan 16	124.636	15.177	24.951	104 ± 8	[2]
(83982) Crantor	2002 May 14	85.232	14.042	19.367	59 ± 12	[2]
(95626)	2019 Aug 29	110.246	17.998	22.992	237 ± 8	[2]
2002 CB$_{249}$	2002 Feb 07	151.521	13.899	28.421	46 ± 17	*
(427507)	1998 Jun 05	103.011	13.933	21.974	40 ± 15	*
(5145) Pholus	1991 Sep 22	91.352	8.653	20.283	99 ± 15	[2]
(7066) Nessus	1992 Jan 18	121.432	11.832	24.522	60 ± 15	[1]
(8405) Asbolus	2002 Jul 28	77.005	6.879	18.100	85 ± 9	[2]
(10199) Chariklo	2003 Dec 04	62.417	13.059	15.735	248 ± 18	[3]
(52872) Okyrhoe	2008 Jan 20	24.071	5.785	8.337	36 ± 1	[1]
(2060) Chiron	1996 Jan 27	50.545	8.486	13.670	218 ± 20	[3]
29P/S-W 1	2019 Apr 15	14.708	5.745	6.003	37 ± 12	[4]
C/1995 O1 (H-B)	1997 Apr 01	2533.975	0.914	185.864	60 ± 20	[5]

Note. The list contains 17 Centaurs in which CO outgassing was searched for and also the long-period comet C/1995 O1 (Hale-Bopp) in which CO outgassing was measured at a range of heliocentric distances characteristic of Centaurs. The data are grouped as in Table 2.
[a]The closest date of perihelion adopted from the JPL Small-Body Database.
[b]Orbital period adopted from the JPL Small-Body Database.
[c]Perihelion distance adopted from the JPL Small-Body Database.
[d]Semimajor axis adopted from the JPL Small-Body Database.
[e]Reference for the diameter: [1] Bauer et al. (2013); [2] Duffard et al. (2014); [3] Fornasier et al. (2013); [4] Stansberry et al. (2008); [5] Campins & Fernández (2002); *Diameter calculated from the absolute visual magnitude of 11.4 ± 0.3 mag for (315898), 9.8 ± 0.3 mag for 2002 CB$_{249}$, and 10.1 ± 0.3 mag for (427507), assuming a geometric albedo of 10 ± 7 per cent, where the uncertainty of the diameter is obtained upon propagating the errors on albedo (enclosing nearly the entire range of literature values, e.g. Duffard et al. 2014) and absolute magnitude (taken from Bauer et al. 2013), and is equal to 37.63 per cent of the diameter for the assumed input errors; **Diameter calculated as an average from the upper limit of 28 km obtained by Jewitt (2009) for the same assumed albedo of 10 per cent as above, and from the lower limit of 2 km which we infer assuming the same activity level per unit nucleus area as of comet Hale-Bopp, which was intrinsically 7.5 mag brighter in total visual magnitude (implying a 30 times bigger nucleus), where the adopted error encloses both limits.

1981). We executed this short procedure every ∼20 min between science integrations and always after moving the antenna to the next target, ensuring in this way that the calibration was up to date.

Throughout the nights we also observed planets: Jupiter or Mars (usually both), which served as compact continuum sources of known fluxes, and also strong compact molecular sources (circumstellar envelopes) associated with late-type stars: the red giant *o* Cet (Mira) or the Mira-type carbon star IZ Peg (usually both), the latter also known as CRL 3099. We used these standard objects to determine and correct for the telescope pointing offsets (every

~2 h), as well as measure the main-beam efficiency η_{mB} (continuum sources) and system stability (all sources). The pointing corrections were very small compared to the telescope beam size, ensuring us that the objects were well centred within the beam with negligible pointing-related signal losses (cf. Drahus et al. 2010, 2011). The average nightly values of η_{mB} turned out to vary between 0.48 and 0.81, but the standard deviation never exceeded 7 per cent during a single night (limited to seven nights when multiple planetary measurements were obtained). After correcting the line standards for the average nightly values of η_{mB}, the stability of the system turns out to be very good, with the baseline-corrected line area of the molecular standards having also only 7 per cent standard deviation in the complete, combined data set of the two reference objects. We attribute the large night-to-night variation of η_{mB} to the loose tertiary mirror, which was repositioned to some degree whenever we removed or mounted the mirror cover during the first four nights. After the mirror was fixed before the fifth night of observation, η_{mB} improved and stabilized, with the average nightly values between 0.73 and 0.81 during the remaining five nights.

For each of the observed Centaurs, the individual spectra from the same night were combined using the GILDAS/CLASS software[3] with the weights proportional to the integration time and inversely proportional to the square of the system temperature. The night-averaged spectra were then calibrated to the scale of the main-beam brightness temperature T_{mB} using the average nightly values of η_{mB}. The corrected spectra have individually subtracted linear baselines, which we fitted in the velocity intervals between -10 and $-2\,\mathrm{km\,s^{-1}}$ and between $+2$ and $+10\,\mathrm{km\,s^{-1}}$. We also used the baseline intervals for the calculation of the noise variance. Then, the spectra from all the nights were combined using inverse-variance weighting. In this way we generated the final spectra for all three Centaurs, which are presented in Fig. 2.

The CO line is undetected in all three objects, with the T_{mB} noise RMS (obtained from the variance) in the original spectral channels equal to 21.6 mK for (315898), 12.5 mK for (342842), and 12.7 mK for (382004). However, our real sensitivity to the CO emission is better parametrized by a 3σ error of the T_{mB} line area in a $0.5\,\mathrm{km\,s^{-1}}$ velocity interval, which encloses practically the entire line (see further in Section 3). Ignoring the uncertainty of baseline subtraction, the standard error of the line area is simply RMS $\times$ $d\nu_r\sqrt{\Delta\nu_r/d\nu_r}$, where $d\nu_r$ is the channel width ($0.0794\,\mathrm{km\,s^{-1}}$ in our case) and $\Delta\nu_r$ is the selected line-area interval ($0.5\,\mathrm{km\,s^{-1}}$). At this point we make no assumption as to the central velocity of this interval. Consequently, we obtain the sensitivities of $4.30\,\mathrm{mK\,km\,s^{-1}}$ for (315898), $2.50\,\mathrm{mK\,km\,s^{-1}}$ for (342842), and $2.53\,\mathrm{mK\,km\,s^{-1}}$ for (382004). These values are listed in Table 2 along with some basic parameters of the observations and the results of subsequent modelling (further discussed in Sections 3 and 4).

2.2 Earlier observations

Given that our project is a continuation of earlier efforts having the same goals (cf. Section 1), we include in the analysis all the previously published observational data on gaseous CO in Centaurs. We therefore take into account the non-detections in seven objects observed by Jewitt et al. (2008) and in five objects observed by Bockelée-Morvan et al. (2001), including Chiron. For the sake of completeness, we also include the less sensitive measurements of Chiron obtained earlier by Rauer et al. (1997) and Womack & Stern
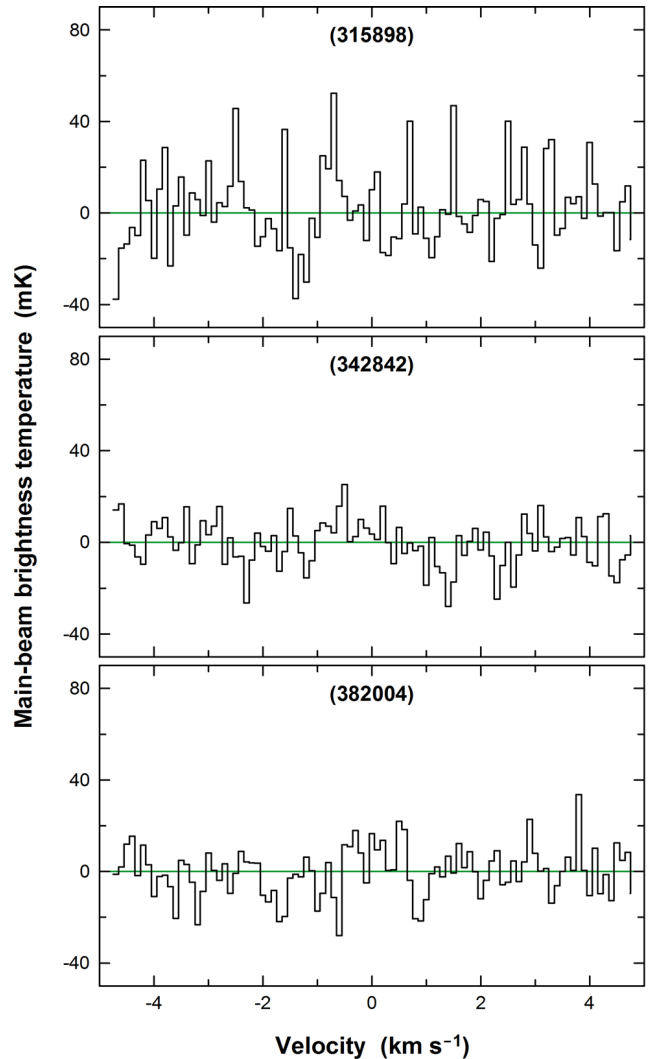
Figure 2. CO $J(2–1)$ spectra of three Centaurs observed by our survey.

(1997). Although the latter authors actually claim a detection of the CO $J(1–0)$ line in their spectra, their inference has been questioned (e.g. Bockelée-Morvan et al. 2001) as based on insufficient signal-to-noise ratio and unconfirmed by subsequent observations. We conservatively consider this observation as a non-detection and use it to constrain another (not very sensitive) upper limit to the outgassing rate of CO in Chiron. We also include 29P, which remains to date the only Centaur with a well-detected (and routinely observed) CO coma. In this case, we separately consider the minimum and maximum production-rate levels reported by Biver (1997), assuming a constant heliocentric distance equal to the value of the orbital semimajor axis (cf. Table 1). Finally, following earlier authors (e.g. Bockelée-Morvan et al. 2001; Jewitt et al. 2008), we include for reference the long-period comet C/1995 O1 (Hale-Bopp), which was monitored in terms of the CO outgassing at large heliocentric distances typical of Centaurs (Biver et al. 2002). The orbital and physical characteristics of all these objects are shown in Table 1.

Whereas the measured CO outgassing rates of 29P and comet Hale-Bopp can be taken directly from the literature, in order to make use of the published non-detections of CO in Centaurs it is necessary to first unify the reported sensitivities, so that they become consistent with the sensitivity defined in Section 2.1. Jewitt et al. (2008) observed CO $J(2–1)$ with the 15 m James Clerk Maxwell

Table 2. Summary of existing data on CO outgassing in Centaurs.

Object	Ref.[a]	Epoch[b]	Telescope	Line	Obs. limit[c]	r[d] (au)	Δ[e] (au)	ϕ[f] (°)	$\log(E_\odot)$[g]	$\log(Q)$[h]	$\log(Q/E_\odot)$[i]
(315898)	[1]	2011 Oct 28.5	CSO 10.4 m	$J(2–1)$	12.89	5.748	5.463	9.7	$10.19^{+0.27}_{-0.39}$	<27.33	$<17.13^{+0.39}_{-0.27}$
(342842)	[1]	2011 Oct 28.6	CSO 10.4 m	$J(2–1)$	7.50	6.576	6.499	8.7	$11.05^{+0.01}_{-0.01}$	<27.12	$<16.08^{+0.01}_{-0.01}$
(382004)	[1]	2011 Oct 27.9	CSO 10.4 m	$J(2–1)$	7.58	6.483	5.666	5.3	$10.05^{+0.08}_{-0.09}$	<27.07	$<17.02^{+0.09}_{-0.08}$
166P/NEAT	[2]	2002 Aug 23.5	JCMT 15 m	$J(2–1)$	19.80	8.571	8.144	6.3	$9.52^{+0.54}_{-1.75}$	<27.38	$<17.87^{+1.75}_{-0.54}$
(60558) Echeclus	[2]	2002 May 29.4	JCMT 15 m	$J(2–1)$	16.03	14.826	14.527	3.8	$10.31^{+0.03}_{-0.03}$	<27.56	$<17.25^{+0.03}_{-0.03}$
(55576) Amycus	[2]	2002 May 25.0	JCMT 15 m	$J(2–1)$	18.86	15.201	14.650	3.2	$10.70^{+0.06}_{-0.07}$	<27.64	$<16.94^{+0.07}_{-0.06}$
(83982) Crantor	[2]	2002 May 22.3	JCMT 15 m	$J(2–1)$	15.08	14.038	13.201	2.4	$10.28^{+0.16}_{-0.20}$	<27.48	$<17.21^{+0.20}_{-0.16}$
(95626)	[2]	2002 May 22.4	JCMT 15 m	$J(2–1)$	15.08	21.123	20.641	2.4	$11.13^{+0.03}_{-0.03}$	<27.81	$<16.68^{+0.03}_{-0.03}$
2002 CB$_{249}$	[2]	2002 Apr 23.4	JCMT 15 m	$J(2–1)$	26.40	13.901	13.269	3.3	$10.07^{+0.27}_{-0.40}$	<27.73	$<17.66^{+0.40}_{-0.27}$
(427507)	[2]	2002 May 30.4	JCMT 15 m	$J(2–1)$	21.68	14.523	14.614	4.0	$9.91^{+0.28}_{-0.41}$	<27.69	$<17.78^{+0.41}_{-0.28}$
(5145) Pholus	[3]	2000 Feb 17.1	JCMT 15 m	$J(3–2)$	28.40	14.851	14.498	3.6	$10.68^{+0.12}_{-0.14}$	<27.83	$<17.16^{+0.14}_{-0.12}$
	[3]	1999 Jun 25.8	CSO 10.4 m	$J(2–1)$	21.30	14.224	13.877	3.9	$10.71^{+0.12}_{-0.14}$	<27.85	$<17.14^{+0.14}_{-0.12}$
	[3]	1999 Feb 28.5	CSO 10.4 m	$J(3–2)$	23.24	13.912	13.311	3.3	$10.73^{+0.12}_{-0.14}$	<27.91	$<17.18^{+0.14}_{-0.12}$
(7066) Nessus	[3]	1999 Jun 25.0	CSO 10.4 m	$J(2–1)$	34.21	15.027	14.042	1.0	$10.23^{+0.19}_{-0.25}$	<28.07	$<17.84^{+0.25}_{-0.19}$
(8405) Asbolus	[3]	1999 Jun 27.3	CSO 10.4 m	$J(2–1)$	27.11	8.839	8.185	5.2	$11.00^{+0.09}_{-0.10}$	<27.71	$<16.71^{+0.10}_{-0.09}$
	[3]	1999 Feb 28.2	CSO 10.4 m	$J(3–2)$	29.69	9.194	8.832	5.9	$10.96^{+0.09}_{-0.10}$	<27.65	$<16.69^{+0.10}_{-0.09}$
(10199) Chariklo	[3]	2000 Jan 04.1	CSO 10.4 m	$J(2–1)$	14.20	13.369	12.707	3.2	$11.57^{+0.06}_{-0.07}$	<27.62	$<16.06^{+0.07}_{-0.06}$
	[3]	2000 Jan 02.5	CSO 10.4 m	$J(3–2)$	37.44	13.370	12.727	3.3	$11.57^{+0.06}_{-0.07}$	<28.08	$<16.51^{+0.07}_{-0.06}$
	[3]	1999 Feb 28.4	CSO 10.4 m	$J(3–2)$	25.82	13.503	12.575	1.5	$11.56^{+0.06}_{-0.07}$	<27.92	$<16.36^{+0.07}_{-0.06}$
	[3]	1998 Nov 26.7	JCMT 15 m	$J(3–2)$	13.56	13.548	13.340	4.1	$11.55^{+0.06}_{-0.07}$	<27.42	$<15.86^{+0.07}_{-0.06}$
	[3]	1998 Nov 15.2	CSO 10.4 m	$J(2–1)$	13.56	13.554	13.539	4.2	$11.55^{+0.06}_{-0.07}$	<27.64	$<16.08^{+0.07}_{-0.06}$
(52872) Okyrhoe	[3]*	1998 Oct 31.9	JCMT 15 m	$J(3–2)$	16.14	10.560	9.852	3.9	$10.09^{+0.02}_{-0.02}$	<27.23	$<17.14^{+0.02}_{-0.02}$
(2060) Chiron	[3]	2000 Jul 26.4	CSO 10.4 m	$J(2–1)$	31.63	10.171	9.522	4.5	$11.69^{+0.08}_{-0.08}$	<27.83	$<16.14^{+0.08}_{-0.08}$
	[3]	1999 Jun 25.9	CSO 10.4 m	$J(2–1)$	30.98	9.511	8.666	3.6	$11.75^{+0.08}_{-0.08}$	<27.78	$<16.03^{+0.08}_{-0.08}$
	[3]	1999 Jun 10.5	JCMT 15 m	$J(2–1)$	8.39	9.487	8.528	2.1	$11.75^{+0.08}_{-0.08}$	<27.02	$<15.26^{+0.08}_{-0.08}$
	[3]	1999 Feb 28.6	CSO 10.4 m	$J(3–2)$	32.27	9.336	9.182	6.1	$11.77^{+0.08}_{-0.08}$	<27.71	$<15.94^{+0.08}_{-0.08}$
	[3]	1998 Mar 25.6	JCMT 15 m	$J(3–2)$	13.56	8.900	8.150	4.4	$11.81^{+0.08}_{-0.08}$	<27.02	$<15.21^{+0.08}_{-0.08}$
	[4]	1995 Nov 16.9	IRAM 30 m	$J(2–1)$	27.76	8.460	9.136	4.7	$11.85^{+0.08}_{-0.08}$	<27.27	$<15.42^{+0.08}_{-0.08}$
	[4]	1995 Nov 16.9	IRAM 30 m	$J(1–0)$	58.74	8.460	9.136	4.7	$11.85^{+0.08}_{-0.08}$	<28.42	$<16.57^{+0.08}_{-0.08}$
	[4]	1995 Sep 21.0	IRAM 30 m	$J(2–1)$	43.89	8.471	9.471	0.6	$11.85^{+0.08}_{-0.08}$	<27.49	$<15.64^{+0.08}_{-0.08}$
	[4]	1995 Sep 21.0	IRAM 30 m	$J(1–0)$	46.48	8.471	9.471	0.6	$11.85^{+0.08}_{-0.08}$	<28.34	$<16.49^{+0.08}_{-0.08}$
	[4]	1995 Jun 25.2	IRAM 30 m	$J(2–1)$	40.67	8.497	8.648	6.7	$11.85^{+0.08}_{-0.08}$	<27.41	$<15.57^{+0.08}_{-0.08}$
	[4]	1995 Jun 25.2	IRAM 30 m	$J(1–0)$	34.86	8.497	8.648	6.7	$11.85^{+0.08}_{-0.08}$	<28.17	$<16.32^{+0.08}_{-0.08}$
	[5]	1995 Jun 12.1	KP 12 m	$J(1–0)$	11.72	8.502	8.443	6.9	$11.85^{+0.08}_{-0.08}$	<28.11	$<16.27^{+0.08}_{-0.08}$
29P/S-W 1	[6]	Minimum				6.003			$10.61^{+0.24}_{-0.34}$	28.30	$17.69^{+0.34}_{-0.24}$
	[6]	Maximum				6.003			$10.61^{+0.24}_{-0.34}$	28.90	$18.29^{+0.34}_{-0.24}$

Note. The data obtained by the three multi-object surveys (this work; Bockelée-Morvan et al. 2001; Jewitt et al. 2008) are grouped by the vertical lines. In a similar way, we group all the data obtained for Chiron and also the established characteristics of 29P.

[a]Reference: [1] this work; [2] Jewitt et al. (2008); [3] Bockelée-Morvan et al. (2001); [4] Rauer et al. (1997); [5] Womack & Stern (1997); [6] Biver (1997).

[b]Middle time of the observing run. Note that many runs spanned over multiple, usually consecutive, dates.

[c]Line-detection limit of the observation. Defined as a 3σ error of the line area (i.e. the main-beam brightness temperature integrated over a 0.5 km s^{-1} velocity interval), and given in mK km s^{-1}.

[d]Mid-run heliocentric distance.

[e]Mid-run geocentric distance.

[f]Mid-run phase angle.

[g]Solar energy flux integrated over the object's surface, given as a logarithm of the value in watts. The uncertainty results entirely from the error on the object's diameter (see Table 1).

[h]3σ upper limit on the CO production rate or the actually measured value (only for 29P), given as a logarithm of the value in molec s^{-1}.

[i]Limit to the CO outgassing rate or the actually measured value (only for 29P) generated in response to each watt of the object-integrated solar energy flux, given as a logarithm of the value in molec s^{-1} W^{-1}.

*This observation suffers from a significant beam offset, leading to the overestimation of the provided sensitivity by ∼30 per cent.

Telescope (JCMT) atop Mauna Kea, publishing 3σ errors of the T_A^* line area in a $1.0\,\mathrm{km\,s^{-1}}$ velocity interval. We recalculate their limits in a $0.5\,\mathrm{km\,s^{-1}}$ interval by dividing by $\sqrt{2}$, and convert to the T_{mB} scale by further dividing by 0.75 (the ratio of η_{mB} to forward efficiency taken from the telescope website, which at JCMT is simply referred to as the main-beam efficiency). Bockelée-Morvan et al. (2001) observed with JCMT and CSO, and Rauer et al. (1997) used the 30 m telescope of the Instituto de Radioastronomía Milimétrica (IRAM) on Pico Veleta. Both teams published their 3σ errors of the line area already in the T_{mB} scale, but derived from a $1.2\,\mathrm{km\,s^{-1}}$ velocity interval, so we recalculate these errors in a $0.5\,\mathrm{km\,s^{-1}}$ interval by dividing by $\sqrt{2.4}$. Bockelée-Morvan et al. (2001) additionally provided beam offsets arising from ephemeris and pointing errors, which they took into account in the calculation of the CO outgassing limits. These offsets are generally small, though, reducing the sensitivities of all but a single observation by <10 per cent, which we calculated with our model (further discussed in the next section). The only observation suffering from a significant beam offset is the one of Okyrhoe, but even in this single case the reduced sensitivity is within ~30 per cent of a well-centred observation, which is probably still small compared to the errors introduced by the poorly known model parameters. For this reason, and for the sake of consistency with the other data sets, we do not take these beam offsets into account in the recalculation of the CO limits from the data of Bockelée-Morvan et al. (2001). As for the sensitivity of Womack & Stern (1997), who observed with the 12 m telescope on Kitt Peak (KP), we estimate the noise RMS in their high-resolution spectrum $T_R^* = 10\,\mathrm{mK}$ in $0.26\,\mathrm{km\,s^{-1}}$ spectral channels. Given that $T_{mB} = T_R^* \, \eta_l \, \eta_{fss}/\eta_{mB}$, where $\eta_l = 0.94$, $\eta_{fss} = 0.68$, and $\eta_{mB} = 0.59$ for this telescope at 115.3 GHz (Mangum 2000), we recalculate the sensitivity in the T_{mB} scale, and further covert to the 3σ error of the line area in a $0.5\,\mathrm{km\,s^{-1}}$ interval in the standard way. After unifying the reported sensitivities, these earlier data were analysed consistently with our new measurements, and therefore are included in Table 2.

3 MODEL OF THE CARBON MONOXIDE RELEASE AND ROTATIONAL EMISSION LINES

In order to convert the achieved sensitivities into upper limits on the CO outgassing rate, we constructed a simple physical model to generate and compare synthetic line profiles with the observational limits. In this section, we only provide a brief overview of the key assumptions and properties of the model. A formal derivation is presented separately in Appendix A.

We start by solving the standard energy budget equation (cf. e.g. Cowan & A'Hearn 1979; Groussin et al. 2013), which balances the incoming energy with the outgoing energy. We assume that the only source of incoming energy is the solar radiation flux, neglecting other sources, either internal (e.g. phase transition or radioactive decay) or external (e.g. cosmic microwave background). Energy release by the crystallization of amorphous ice is potentially an important source (e.g. Prialnik et al. 2008), but crystallization is extremely temperature-dependent and occurs locally and episodically on any given nucleus (Guilbert-Lepoutre 2012). In our model, the outgoing energy is initially partitioned into the energy flux reflected off the surface, the energy flux thermally radiated by the surface, and the energy flux used for breaking bonds between molecules in sublimation. We neglect the outgoing energy in the form of heat conduction into the interior bearing in mind the very low heat conductivity of cometary nuclei, of the order of 10^{-3} to $10^{-2}\,\mathrm{W\,m^{-1}\,K^{-1}}$ (e.g.
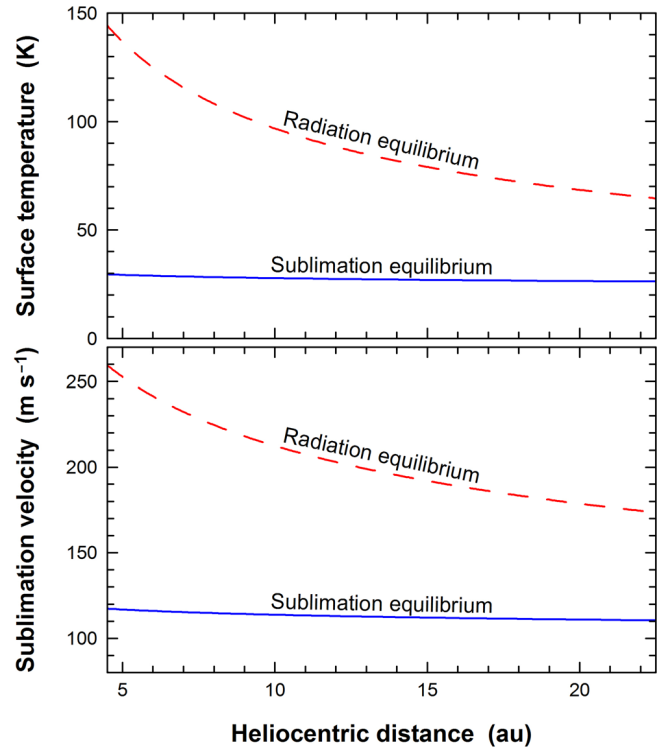

Figure 3. Summary of physical conditions applicable to the surfaces and CO atmospheres of Centaurs. We show the average equilibrium temperature of the illuminated hemisphere (top panel) and the thermal velocity of CO corresponding to this temperature (bottom panel) for two different situations. For equilibrium with radiation (red line) we assume that 10 per cent of the incoming solar energy is reflected back to space and the rest is absorbed and thermally re-radiated, whereas for equilibrium with sublimation (blue line) 70 per cent of the energy is reflected and the rest is used for the sublimation of CO. The derived dependencies only weakly depend on the assumed albedo. In both cases, the Sun is assumed to be the only source of incoming energy.

Kührt 1999; Groussin et al. 2013). Assuming that the considered objects are spherical, we note that the incident solar radiation flux varies across the day side in proportion to the cosine of the solar zenith angle. To account for this effect, we divide the surface into small elements defined by a $1° \times 1°$ spherical grid, and solve the budget equation for each surface element separately, assuming no heat exchange between the elements.

With the aid of the Clausius–Clapeyron formula, we first solve the budget equation for temperature assuming a high Bond albedo of CO ice $A = 70$ per cent, and then calculate the mean day-side surface temperature. It is easy to check that at the heliocentric distances characteristic of Centaurs nearly all the absorbed energy is instantly used for sublimation and the radiative losses are completely negligible, which is due to the extreme volatility of CO. Strictly speaking, with the adopted albedo the object-integrated radiative losses are between a factor of 8.3 (at the distance of Neptune) and a factor of 180 (at the distance of Jupiter) smaller than the corresponding losses for CO sublimation. For comparison, we also calculate the average day-side temperature of a refractory surface with a low albedo $A = 10$ per cent. In Fig. 3, we show the temperature dependence on heliocentric distance and the corresponding bulk (i.e. average) sublimation velocity normal to the surface $v_{subl} = \sqrt{\pi k_B T_{sf}/(2\,\mu)}$ (Huebner & Markiewicz 2000), where k_B is the Boltzmann constant and μ is the mass of a single molecule. It can be readily seen that the temperature in equilibrium with CO sublimation is nearly constant at ~30 K throughout the entire region occupied by Centaurs, and so

is the corresponding thermal velocity, which we find to be equal to $\sim$115 m s^{-1}. However, in the absence of sublimation, the refractory surface reaches considerably higher temperatures and associated thermal velocities, and the dependence on heliocentric distance is no longer negligible.

From now on we will consistently assume that the surface is made of pure CO ice and, neglecting the energy flux thermally radiated, solve the budget equation for the sublimation flux. We find the sublimation flux to be proportional to the solar energy flux (which is proportional, on the day side, to the cosine of the solar zenith angle, and inversely proportional to the square of the heliocentric distance), which implies that non-zero sublimation is restricted to the day side. The sublimation flux is then integrated over the day side, which gives the total CO production rate. We also constrain a three-dimensional density function of the CO coma, assuming that the molecules sublimate normally to the surface, continue to travel along straight lines at a constant velocity, and that this velocity is isotropic. Additionally, we take into account the finite photochemical lifetime of the molecules, which is equal to 211.326 h for CO gas at 1 au from the Sun (Huebner, Keady & Lyon 1992), and proportional to the square of the heliocentric distance. Note, however, that this process is completely negligible (for any realistic gas flow velocity) on the length scales characteristic of the telescope beam sizes used for the observations of Centaurs. It is easy to recognize that our coma model is a steady-state anisotropic construction, which is identical with the time-dependent anisotropic model of Drahus (2009) for objects with uniform volatility ('sublimation potential').

Next, we calculate a synthetic spectrum for every volume element in the coma, which is simply given by the *spectral emissivity*. The emitted power is a product of the transition energy (related to the transition rest frequency by the Planck constant), transition rate (given by the Einstein coefficient for spontaneous emission), and the number of molecules occupying the upper energy level. The power distribution across the frequency is given by a normalized function, controlled, through the Doppler effect, by the velocity distribution of the molecules. It is customary in radio astronomy to replace the power with the brightness temperature, and change the frequency domain for radial velocity. The former conversion is obtained using the Rayleigh–Jeans approximation and the latter through the Doppler law. Working from now on in the radial-velocity domain, we assume that each volume element generates a Gaussian line profile, resulting from the Maxwell–Boltzmann distribution of the velocity vector in a single direction. The line is centred in the spectrum at the velocity equal to the gas-flow velocity component along the line of sight, and has a width controlled by the gas temperature.

Assuming that the coma is optically thin at the observed frequency, the radiative transfer problem simplifies to integrating the brightness temperature generated by all individual volume elements. For the sake of simplicity and clarity in the model derivation (Appendix A), the integration is performed in the cylindrical coordinate system. We first integrate in one dimension along lines parallel to the line of sight. Then the resulting column-integrated brightness temperature is weighted by and integrated in two dimensions over the main-beam profile, and normalized by the integrated beam profile. The resulting quantity is the main-beam brightness temperature T_{mB}, which represents the spectrum of the entire expanding coma as seen by the telescope beam. However, in our numerical implementation, the integration is performed in the spherical coordinate system, after dividing the coma into small volume elements defined by a $1° \times 1° \times 10$ km spherical grid.

Synthetic CO spectra of the Centaurs were consistently calculated for the gas flow velocity of 200 m s^{-1} and the gas temperature

of 10 K, both assumed to be constant everywhere in the coma. The adopted gas temperature is lower than the calculated average surface temperature of $\sim$30 K on the day side because the coma is expected to adiabatically cool as the gas travels away from the nucleus, and photolytic heating in the outer coma is thought to be negligible for weakly sublimating objects (Combi, Harris & Smyth 2004). Moreover, gas temperatures of 5–10 K were measured for CO at the heliocentric distances characteristic of Centaurs in comet Hale-Bopp (Biver et al. 2002) and active Centaur 29P (Crovisier et al. 1995; Paganini et al. 2013). The assumed gas flow velocity is somewhat higher than the calculated average sublimation velocity of $\sim$115 m s^{-1} (corresponding to the mean surface temperature on the day side), but is lower than the velocity of $\sim$500 m s^{-1}, measured at comparable heliocentric distances in Hale-Bopp (Biver et al. 2002) and 29P (Crovisier et al. 1995). We chose the intermediate value because, on the one hand, the gas is expected to accelerate after leaving the nucleus (Combi et al. 2004), but on the other hand, the efficiency of this process should be lower in the (at most) weakly sublimating Centaurs than in the dense comae of Hale-Bopp and 29P. It is worth noting that although in our calculation we assumed the gas temperature to be constant everywhere in coma, this assumption is not really required by the model, unlike the assumed constant gas flow velocity, which simplifies the model considerably. The energy-level population is calculated assuming fluorescence equilibrium (FE), following the same approach as Crovisier & Le Bourlot (1983) and Chin & Weaver (1984). FE should better characterize the non-detected (supposedly low-density) CO comae of Centaurs than the traditionally assumed thermodynamic equilibrium (TE) established by molecular collisions. In Fig. 4, we show the fractional occupancy of the energy levels of interest in TE (as a function of gas temperature) and in FE (as a function of heliocentric distance), and note that the differences are generally not very significant in the parameter space characteristic of Centaurs.

In Fig. 5, we show two examples of spectra generated with our model: one for anisotropic outgassing assumed in this work, and the other one for isotropic outgassing conventionally assumed in all previous searches for gaseous CO in Centaurs (Senay & Jewitt 1994; Rauer et al. 1997; Womack & Stern 1997; Bockelée-Morvan et al. 2001; Jewitt et al. 2008) and in the vast majority of similar works on comets (e.g. Bockelée-Morvan et al. 2004), including our earlier publications (e.g. Drahus et al. 2010, 2011, 2012). Unsurprisingly, the line areas in both examples are comparable, but the anisotropic model predicts a much more narrow and asymmetric line profile, consistent with the basic characteristics of the velocity-resolved CO spectrum of 29P (e.g. Crovisier et al. 1995; Festou et al. 2001). A velocity interval of 0.5 km s^{-1}, assumed in the calculation of the observational limits (cf. Section 2), contains as much as 99.97 per cent of the line area in the adopted anisotropic scenario (if integrated from -0.38 to $+0.12$ km s^{-1}), and 94.5 per cent of the line area in the isotropic case (if integrated from -0.25 to $+0.25$ km s^{-1}). Here we assume for simplicity that the entire line is in that interval. Admittedly, a choice of an even more narrow velocity interval, enclosing a smaller fraction of the line area but measured with a significantly smaller error, would result in a higher signal-to-noise ratio (or a lower outgassing-rate limit), especially for the assumed anisotropic case. However, we conservatively calculate the limits in a 0.5 km s^{-1} interval to make the results valid also for somewhat broader lines, due to e.g. a higher gas velocity or more complicated outgassing pattern (such as a likely combination of Sun-facing and isotropic components). In that case, if the outgassing rate is equal to the calculated limit, a broader line may still
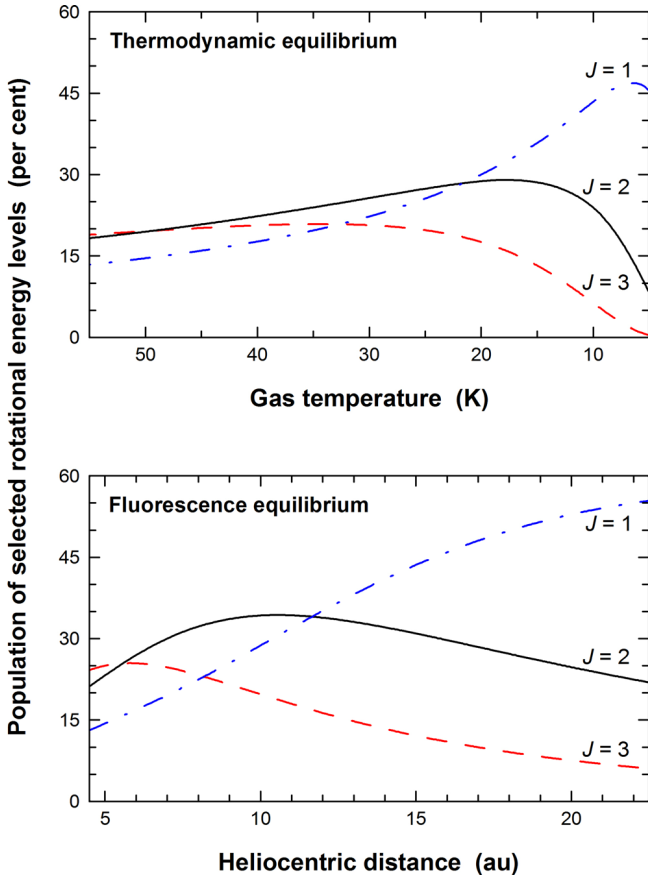
Figure 4. Population of $J = 1$, 2 and 3 rotational energy levels of CO in the ground electronic and vibrational state, corresponding to the upper levels of the transitions which were searched for in Centaurs (see Table 2). We show the calculations both for TE (top panel), in which the energy levels are occupied according to the Maxwell–Boltzmann distribution controlled by the gas temperature, and also for the FE (bottom panel) assumed in this work, in which the population is established by the solar flux density controlled by the heliocentric distance.

be detected at or closer to the assumed 3σ level (cf. Section 2), but in a more narrow velocity interval.

By choosing the anisotropic outgassing, the recalculated sensitivities from the previous surveys turn out to be higher than those originally inferred from the wider velocity intervals (cf. Section 2.2). This leads to significant differences between the recalculated and original production-rate limits, with additional effects arising from the difference between the model line areas, assumed rotational populations and especially gas velocities, and also different treatments of the beam offsets.

4 LIMITS TO THE CARBON MONOXIDE PRODUCTION RATE AND DISCUSSION

Using the model introduced in the previous section, we converted the observational limits on the line area into the corresponding 3σ limits on the CO production rate Q. These limits are summarized in Table 2 for all the Centaurs considered in this work, including the production-rate range of 29P taken from the literature. In particular, for the three objects observed by our survey we obtained $Q < 2.13 \times 10^{27}$ molec s^{-1} for (315898), $Q < 1.32 \times 10^{27}$ molec s^{-1} for (342842), and $Q < 1.17 \times 10^{27}$ molec s^{-1} for (382004).
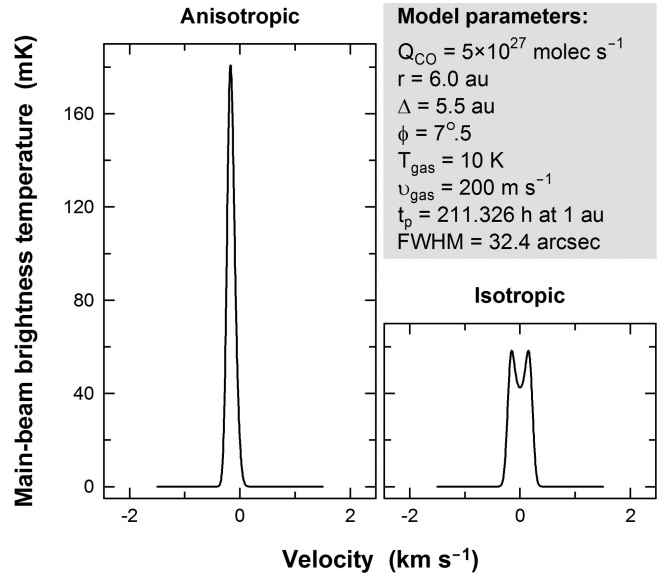
Figure 5. Model of the CO $J(2–1)$ line profile in FE, calculated for an arbitrary production rate Q_{CO}. The observing geometry, represented by the heliocentric distance r, geocentric distance Δ, and phase angle ϕ, is chosen to be typical of Centaurs, and the assumed gas temperature T_{gas} and gas velocity υ_{gas} are thought to be likewise. The model takes into account finite photochemical lifetime of the molecules t_p, and was calculated for the beam FWHM of the CSO. We show the results for anisotropic outgassing from the day side (left-hand panel) assumed in this work and also for isotropic outgassing (right-hand panel) which has been commonly assumed in earlier works. Note that although the line areas are comparable, and equal to 5.6mK km s^{-1} for anisotropic outgassing and 4.4mK km s^{-1} for isotropic outgassing, the two line profiles look dramatically different.

Before analysing the results, it is interesting to first review the investigated objects in the parameter space of their diameters and heliocentric distances (at the epochs of the observations), which is presented in Fig. 6. This space is special because, according to our simple model (Section 3), the CO production rate Q is inversely proportional to the square of the heliocentric distance and directly proportional to the square of the diameter if the ice fraction is constant over the surface. Note that these relations imply that Q is directly proportional to the solar energy flux integrated over the object's surface $E_\odot$ (cf. Appendix A), a quantity also presented in Fig. 6. The figure shows that the objects differ by two orders of magnitude in terms of $E_\odot$. All of the largest ones, with diameters >200 km, have also the highest $E_\odot > 10^{11}$ W. However, two much smaller objects, with diameters <100 km, including (342842) observed by our survey, also have a high $E_\odot \sim 10^{11}$ W, owing to their small heliocentric distances. In fact, all the three objects from our survey are particularly interesting in that they were observed at the smallest heliocentric distances in the considered group, comparable only to the heliocentric distance of 29P. To be specific, the heliocentric distance of (315898) was essentially the same as the perihelion distance of 29P, and the heliocentric distances of (342842) and (382004) were only slightly greater than the aphelion distance of 29P. In terms of their diameters, (315898) and (382004) are about half the size of 29P, which places them among the smallest objects in the considered group. But (342842) is much bigger, nearly twice the size of 29P, which, combined with the small heliocentric distance, results in the relatively high $E_\odot \sim 10^{11}$ W.

With these properties in mind, let us now analyse the CO production rates (29P and Hale-Bopp) and the calculated upper limits (all
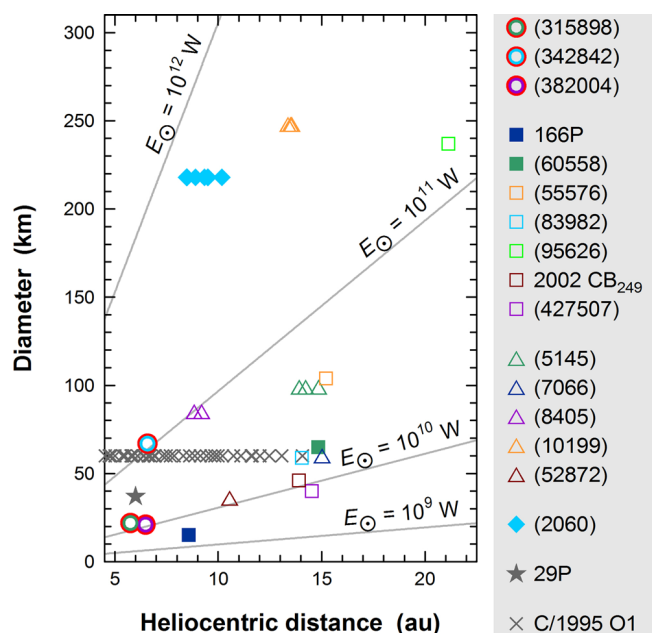
Figure 6. Observations of the Centaurs considered in this work, presented in the space of two independent variables, diameter and heliocentric distance, which control the object-integrated solar energy flux $E_\odot$ (solid lines). The individual Centaurs are represented by closed-shape symbols, one per observation, which distinguish the objects that appear active in the optical (filled symbols) from the objects that have not been seen active (unfilled symbols). We include both the new data obtained in the course of our survey (red-envelope circles) and also the data obtained earlier (other symbols). For comparison, we also include the data for the long-period comet C/1995 O1 (Hale-Bopp), which was observed in CO in the considered range of heliocentric distances (open-shape symbol). The different data sets are grouped in the legend and share the same symbol shape. See Tables 1 and 2 for details and references.

the other objects) as a function of $E_\odot$, which is presented in Fig. 7. It is visible that the most sensitive searches reached a production-rate limit of $\sim 1 \times 10^{27}$ molec s^{-1}, achieved by our survey for (342842) and (382004), and earlier by the deepest observations of Chiron. As for the third object that we observed, (315898), the limit is twice as large, but still very tight. Such a level of CO outgassing is one to two orders of magnitude lower than the CO production rate routinely measured in 29P. The difference becomes even more pronounced when we consider the outgassing rate normalized by the object-integrated solar energy flux $E_\odot$, which is also presented in Fig. 7. Then the CO outgassing from 29P appears to be two to three orders magnitude more efficient, and the CO outgassing of Hale-Bopp about two orders magnitude more efficient, than allowed by the most stringent limit for Chiron. Our own limit for (342842), though not as tight in terms of the outgassing efficiency, is also among the most sensitive achieved to date.

At this point we must note that it is unclear whether the CO outgassing rate Q of Centaurs should be indeed correlated with the object-integrated solar energy flux $E_\odot$. On the one hand, this simple relation resulting from our sublimation model was very closely followed by comet Hale-Bopp, which consistently produced about 3×10^{17} molecules of CO in response to each watt of the object-integrated solar energy flux. In fact, this behaviour approximately continued all the way to and from perihelion at 0.914 au, spanning over several orders of magnitude (Biver et al. 2002). On the other hand, the amount of CO on the surfaces of Centaurs may not be correlated with the surface area, differentiating the objects in terms of
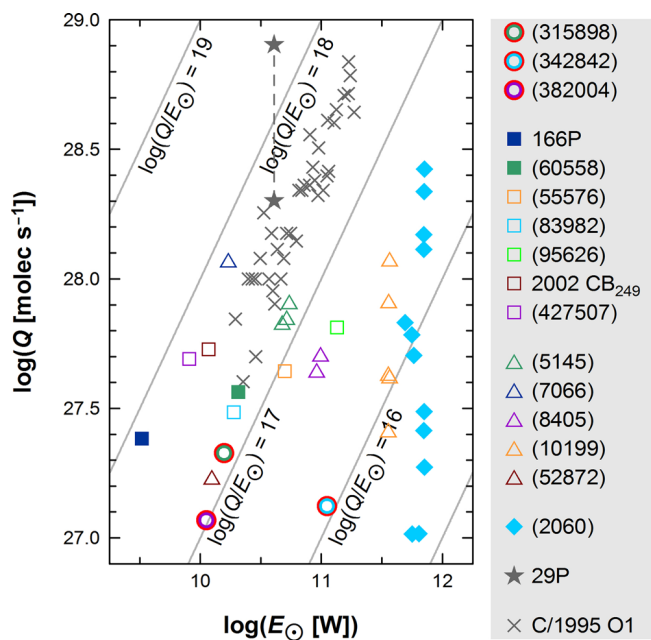

Figure 7. Results of this and previous surveys. The 3σ upper limits on the CO production rate Q or the actually measured values of Q (only for 29P and C/1995 O1) are displayed against the object-integrated solar energy flux $E_\odot$ at the epoch of the observation. Both quantities are given as logarithms, and their ratio is shown by the solid lines, also as logarithm. The meaning of the symbols is the same as in Fig. 6.

the ice fraction. We can also easily imagine that the CO ice is present only beneath the surface. In that case, a strong and persisting solar energy flux is more important than a high object-integrated flux (naturally satisfied by large objects), so that the heat can propagate deep enough to initiate sublimation. This requires small heliocentric distances, and ideally also small semimajor axes, rather than large diameters. Indeed, the four Centaurs in the considered sample that ever showed cometary activity (filled symbols in Figs 6 and 7) are scattered across the entire range of $E_\odot$, with Chiron having the highest and 166P the lowest values at the epochs of the observations (although the size, and hence $E_\odot$, are extremely uncertain for 166P; see Table 1), but they seem to be closer to the Sun than the Centaurs that have never been seen active. (We neglect here the fact that the figures represent the moments of CO searches in these objects whereas their cometary activity might have been observed at somewhat different times.) A statistical tendency of optically active Centaurs to have smaller perihelion distances (and be observed as active at smaller heliocentric distances) than inactive Centaurs was also noticed earlier by Jewitt (2009) in a bigger sample. If we assume that the level of optical activity (or, more precisely, dust production rate) is correlated in these objects with the CO production rate, this may suggest that indeed a small heliocentric distance is more important to initiate the sublimation of CO than the object's large size. However, the latter assumption is seemingly inconsistent with the poor (if any) correlation between these two quantities in 29P, and the optical activity of Chiron is clearly uncorrelated with the heliocentric distance (for 29P the heliocentric range is too limited to allow for any inference in this regard). Moreover, the three Centaurs that we observed were located at the smallest heliocentric distances in the considered group, but despite achieving the exceptionally high sensitivity to CO outgassing, we could not see the slightest sign of it in our data. Altogether, these facts show that the issue is open and still poorly understood (cf. Section 1).

5 SUMMARY AND CONCLUSIONS

In spite of nearly two decades of efforts and investigating 17 individual objects, CO outgassing remains undetected in any Centaur other than 29P. In this work we presented new limits obtained for three objects: (315898), (342842), and (382004), and also reevaluated all previously published observational results. The most sensitive constraint on the CO production rate is the level $\sim 1 \times 10^{27}$ molec s^{-1}, obtained for Chiron from the data of Bockelée-Morvan et al. (2001), and for (342842) and (382004) from the new data presented in this work. The limit for the third object that we observed, (315898), though twice as large, is also among the most sensitive obtained to date. This is to be compared with the production rate 2 to 8×10^{28} molec s^{-1} (Biver 1997) routinely measured in 29P since the first detection by Senay & Jewitt (1994). We therefore reiterate the earlier conclusion by Jewitt et al. (2008) that the surfaces of most Centaurs cannot be dominated by exposed CO ice. In the extreme case, if we calculate with the model from Section 3 the expected CO production rate generated by a spherical object of the size of Chiron with the surface entirely made of CO ice (assumed 70 per cent Bond albedo), we obtain that the observational limit is only 7×10^{-5} of that value, which can be considered as the maximum possible 'active fraction' of the surface for the sublimation of CO (cf. e.g. A'Hearn et al. 1995; Jewitt et al. 2008). The limits for the other objects, though not nearly as low, also support this conclusion.

While exposed CO ice is observationally excluded, CO trapped in amorphous water ice might be released upon its transformation to the crystalline form. The crystallization rate is a strong function of temperature and hence of heliocentric distance, falling to negligible values beyond about 12 au (Jewitt 2009; Guilbert-Lepoutre 2012). Crystallization is also expected to occur episodically, perhaps driving outbursts for which 29P, for example, is well known. Thus, there remains hope that CO might be detected even in objects in which it has been previously sought but not found.

Whether or not we are anywhere near detecting CO gas in a second Centaur, it is clear that the new instrumentation (ALMA, LMT) is already capable (or will be soon) of pushing the limit by an order of magnitude or more within a few days of observation. Consider for example the 50-m LMT (Large Millimeter Telescope). Once eventually operational with its entire reflecting surface fully installed, and equipped with a 1.3 mm dual-polarization sideband-separating SIS receiver, this facility will provide a factor of ~ 7 improvement in sensitivity to CO J(2–1) compared to CSO with Z-Rex, which we used to obtain the state-of-the-art limits presented in this work. An even greater improvement can be expected from ALMA (Atacama Large Millimeter/submillimeter Array) owing to its unparalleled sensitivity at millimetre and submillimetre wavelengths. We can therefore soon expect a breakthrough, especially if large amounts of observing time are allocated to observe selected Centaurs, preferably optically active and close to the inner boundary of the Centaur region.

REFERENCES

A'Hearn M. F., Millis R. L., Schleicher D. G., Osip D. J., Birch P. V., 1995, Icarus, 118, 223
Bauer J. M. et al., 2013, ApJ, 773, 22
Biver N., 1997, PhD thesis, Univ. Paris
Biver N., 2001, Int. Comet Q., 23, 85
Biver N. et al., 1996, Nature, 380, 137
Biver N. et al., 2002, Earth Moon Planets, 90, 5
Bockelée-Morvan D., Lellouch E., Biver N., Paubert G., Bauer J., Colom P., Lis D. C., 2001, A&A, 377, 343
Bockelée-Morvan D., Crovisier J., Mumma M. J., Weaver H. A., 2004, in Festou M. C., Keller H. U., Weaver H. A., eds, Comets II. Univ. Arizona Press, Tucson, AZ, p. 391
Bus S. J., Bowell E., French L. M., 1988, IAU Circ., 4684, 2
Bus S. J., A'Hearn M. F., Schleicher D. G., Bowell E., 1991, Science, 251, 774
Campins H., Fernández Y., 2002, Earth Moon Planets, 89, 117
Chin G., Weaver H. A., 1984, ApJ, 285, 858
Cochran A., Barker E. S., Cochran W., 1980, AJ, 85, 474
Combi M. R., Harris W. M., Smyth W. H., 2004, in Festou M. C., Keller H. U., Weaver H. A., eds, Comets II. Univ. Arizona Press, Tucson, AZ, p. 523
Cowan J. J., A'Hearn M. F., 1979, Moon Planets, 21, 155
Crovisier J., 1993, in Huebner W. H., Jewitt D., Keller H. U., Klinger J., eds, Workshop on the Activity of Distant Comets. Southwest Res. Inst., San Antonio, p. 153
Crovisier J., Le Bourlot J., 1983, A&A, 123, 61
Crovisier J., Biver N., Bockelée-Morvan D., Colom P., Jorda L., Lellouch E., Paubert G., Despois D., 1995, Icarus, 115, 213
Drahus M., 2009, PhD thesis, Univ. Göttingen
Drahus M., Küppers M., Jarchow C., Paganini L., Hartogh P., Villanueva G. L., 2010, A&A, 510, A55
Drahus M. et al., 2011, ApJ, 734, L4
Drahus M., Jewitt D., Guilbert-Lepoutre A., Waniak W., Sievers A., 2012, ApJ, 756, 80
Duffard R., Lazzaro D., Pinto S., Carvano J., Angeli C., Alvarez-Candal A., Fernández S., 2002, Icarus, 160, 44
Duffard R. et al., 2014, A&A, 564, A92
Festou M. C., Gunnarsson M., Rickman H., Winnberg A., Tancredi G., 2001, Icarus, 150, 140
Fornasier S. et al., 2013, A&A, 555, A15
Giorgini J. D. et al., 1997, BAAS, 28, 1099
Groussin O. et al., 2013, Icarus, 222, 580
Guilbert-Lepoutre A., 2012, AJ, 144, 97
Haser L., 1957, Bull. Cl. Sci. Acad. R. Belg., 43, 740
Huebner W. F., Markiewicz W. J., 2000, Icarus, 148, 594
Huebner W. F., Keady J. J., Lyon S. P., 1992, Ap&SS, 195, 1
Jewitt D., 1990, ApJ, 351, 277
Jewitt D., 2009, AJ, 137, 4296
Jewitt D., Luu J., 1993, Nature, 362, 730
Jewitt D. C., Luu J. X., 1995, AJ, 109, 1867
Jewitt D., Senay M., Matthews H., 1996, Science, 271, 1110
Jewitt D., Garland C. A., Aussel H., 2008, AJ, 135, 400
Kopp G., Lean J. L., 2011, Geophys. Res. Lett., 38, L01706
Kowal C. T., Gehrels T., 1977, IAU Circ., 3129, 1
Kührt E., 1999, Space Sci. Rev., 90, 75
Kutner M. L., Ulich B. L., 1981, ApJ, 250, 341
Larson S. M., 1980, ApJ, 238, L47
Levison H. F., Duncan M. J., 1997, Icarus, 127, 13

Mangum J. G., 2000, User's Manual for the NRAO 12 Meter Millimeter-Wave Telescope. Available at: http://aro.as.arizona.edu/12m_docs/12m_userman.pdf

Meech K. J., Belton M. J. S., 1989, IAU Circ., 4770, 1

Meech K. J., Belton M. J. S., Mueller B. E. A., Dicksion M. W., Li H. R., 1993, AJ, 106, 1222

Müller H. S. P., Schlöder F., Stutzki J., Winnewisser G., 2005, J. Mol. Struct., 742, 215

Paganini L. et al., 2013, ApJ, 766, 100

Prialnik D., Sarid G., Rosenberg E. D., Merk R., 2008, Space Sci. Rev., 138, 147

Rabinowitz D., Schwamb M. E., Hadjiyska E., Tourtellotte S., 2012, AJ, 144, 140

Rauer H. et al., 1997, Planet. Space Sci., 45, 799

Senay M. C., Jewitt D., 1994, Nature, 371, 229

Stansberry J., Grundy W., Brown M., Cruikshank D., Spencer J., Trilling D., Margot J.-L., 2008, in Barucci M. A., Boehnhardt H., Cruikshank D. P., Morbidelli A., eds, The Solar System Beyond Neptune. Univ. Arizona Press, Tucson, AZ, p. 161

Tholen D. J., Hartmann W. K., Cruikshank D. P., 1988, IAU. Circ., 4554, 2

Trigo-Rodríguez J. M., García-Melendo E., Davidsson B. J. R., Sánchez A., Rodríguez D., Lacruz J., de Los Reyes J. A., Pastor S., 2008, A&A, 485, 599

Trigo-Rodríguez J. M., García-Hernández D. A., Sánchez A., Lacruz J., Davidsson B. J. R., Rodríguez D., Pastor S., de Los Reyes J. A., 2010, MNRAS, 409, 1682

Ulich B. L., Haas R. W., 1976, ApJS, 30, 247

Womack M., Stern S. A., 1997, Lunar Planet. Sci. Conf., 28, 1575

APPENDIX A: DERIVATION OF ROTATIONAL LINE PROFILES

In this section, we provide a formal derivation of the rotational line profiles applicable to Centaurs, which supplements the discussion presented in Section 3.

A1 Energy budget

We start from the standard energy budget equation on a surface element dS:

$$\frac{dE_{\odot}}{dS} = \frac{dE_{ref}}{dS} + \frac{dE_{rad}}{dS} + \frac{dE_{subl}}{dS}, \tag{A1}$$

which balances the solar energy flux $dE_{\odot}/dS$ with the losses for reflection dE_{ref}/dS, re-radiation dE_{rad}/dS, and sublimation dE_{subl}/dS. The solar energy flux depends on the heliocentric distance r and the solar zenith angle $z_{\odot}$, and is given by

$$\frac{dE_{\odot}}{dS} = \begin{cases} L_{\odot}(r_0)\frac{r_0^2}{r^2}\cos z_{\odot} & \text{for } z_{\odot} \leq 90° \text{ (day side)}, \\ 0 & \text{for } z_{\odot} > 90° \text{ (night side)}, \end{cases} \tag{A2}$$

where $L_{\odot}(r_0)$ is the solar constant, equal to 1361.5 W m^{-2} at $r_0 = 1$ au (Kopp & Lean 2011). The energy flux reflected back to space is

$$\frac{dE_{ref}}{dS} = A\frac{dE_{\odot}}{dS}, \tag{A3}$$

where A is the Bond albedo. The energy flux emitted as thermal radiation is

$$\frac{dE_{rad}}{dS} = \sigma_{SB} T_{sf}^4, \tag{A4}$$

where $\sigma_{SB} = 5.670373 \times 10^{-8}$ W m^{-2} K^{-4} is the Stefan–Boltzmann constant, and T_{sf} is the surface temperature of the con-

sidered surface element dS established by the energy balance. The energy flux consumed for sublimation is

$$\frac{dE_{subl}}{dS} = H\mu\frac{dQ}{dS}, \tag{A5}$$

where dQ/dS is the sublimation flux, and $H = \beta k_B/\mu$ is the latent heat (energy per unit mass) of sublimation, which can be calculated by substituting the gas constant $\beta = 764.16$ K applicable to CO, the mass of a single molecule μ, equal to 4.651186×10^{-26} kg for CO, and the Boltzmann constant $k_B = 1.3806488 \times 10^{-23}$ J K^{-1}. Note that dQ is the sublimation rate and $\mu\,dQ$ is the mass-loss rate generated by the considered surface element dS.

The sublimation flux can be calculated by solving the Clausius–Clapeyron formula, which yields

$$\frac{dQ}{dS} = \frac{P(T_{sf})}{\sqrt{2\pi k_B T_{sf}\mu}}, \tag{A6}$$

where $P(T_{sf}) = \alpha\,e^{-\beta/T_{sf}}$ is the saturated vapour pressure, which can be calculated for CO with the value of β given above and the gas constant $\alpha = 1.2631 \times 10^9$ N m^{-2}.

A2 Outgassing rate and density distribution in the coma

From now on we will only consider the equilibrium with sublimation, in which the energy-budget equation simplifies to $dE_{\odot} = dE_{ref} + dE_{subl}$, which is relevant to our deep search for CO outgassing in Centaurs. Substituting equations (A2), (A3), and (A5), we rewrite this equation as

$$dQ = \frac{1-A}{H\mu}dE_{\odot}$$

$$= \frac{1-A}{H\mu}L_{\odot}(r_0)\frac{r_0^2}{r^2}\cos z_{\odot}dS \quad \text{for } z_{\odot} \leq 90° \text{ (day side)}, \tag{A7}$$

noting that the sublimation rate is proportional to the solar energy rate $dE_{\odot}$ and that non-zero sublimation is restricted to the day side.

It is now desirable to derive the total (i.e. body-integrated) production rate Q, considering a spherical object made of CO ice. First, we note that $\cos z_{\odot} = \cos\theta\cos\varphi$ and $dS = R^2\cos\theta\,d\theta\,d\varphi$, where R is the radius of the object and θ and φ are, respectively, the elevation and azimuth angles in a left-handed spherical coordinate system oriented such that $\theta = 0$ indicates the Sun–object–Earth plane with $\varphi = 0$ indicating the Sunward direction. Consequently, we integrate equation (A7) over the day side:

$$Q = \frac{1-A}{H\mu}R^2 L_{\odot}(r_0)\frac{r_0^2}{r^2}\int_{-\frac{\pi}{2}}^{+\frac{\pi}{2}}\int_{-\frac{\pi}{2}}^{+\frac{\pi}{2}}\cos^2\theta\,\cos\varphi\,d\theta\,d\varphi$$

$$= \frac{1-A}{H\mu}\pi R^2 L_{\odot}(r_0)\frac{r_0^2}{r^2}. \tag{A8}$$

After substituting the above equation in equation (A7), we obtain the sublimation rate dQ normalized by the total production rate Q:

$$dQ = \frac{Q}{\pi}\cos^2\theta\,\cos\varphi\,d\theta\,d\varphi \quad \text{for } -90° \leq \varphi \leq +90° \text{ (day side)}, \tag{A9}$$

which we will use to derive the volume density distribution of the considered molecular gas as a function of the location in the coma. First note that dQ is the sublimation rate into a cone, with a vertex at the centre of the object and a cross-section defined by the sublimating surface element dS. Now consider a volume

element limited by the walls of this cone and located at a distance corresponding to the gas flow time t. The number of molecules inside this element is $dn = dQ\, dt\, e^{-t/t_p}$, where dt is the crossing time of the considered volume element and the exponential term introduces photodestruction of the molecules dependent on the characteristic photochemical lifetime t_p. This lifetime scales with the heliocentric distance r like $t_p \propto r^2$, and is equal to 211.326 h for CO at $r = 1$ au (Huebner et al. 1992). It is convenient to replace the time t with the distance from the object's centre ρ, introducing the gas flow velocity $\upsilon_{gas} = d\rho/dt$. Assuming for simplicity that this velocity is constant everywhere in the coma, we find that $t = (\rho - R)/\upsilon_{gas}$ and $t_p = \rho_p/\upsilon_{gas}$, where ρ_p is the photodissociation scalelength, but also note that $t/t_p = (\rho - R)/\rho_p \approx \rho/\rho_p$, since $\rho_p \gg R$ in most applications. Finally, given that the volume density is $\varrho_v \equiv dn/dV$, where $dV = \rho^2 \cos\theta\, d\rho\, d\theta\, d\varphi$ is the volume element, we use equation (A9) to obtain the density profile for the considered outgassing model:

$$\varrho_v(\rho, \theta, \varphi) = \frac{Q}{\pi\, \rho^2\, \upsilon_{gas}}\, \cos\theta \cos\varphi\, e^{-\rho/\rho_p}$$

$$\text{for } -90° \leq \varphi \leq +90° \text{ (day side).} \qquad (A10)$$

It is also customary to transform the above function to a cylindrical coordinate system oriented along the line of sight. In these new coordinates, we distinguish the distance component along the line of sight s, which can be positive or negative and increases in the Earthward direction, and the (positive) distance component normal to the line of sight ς. The latter is oriented in a position angle ε, which is measured from the Sun–object–Earth plane in the same sense as θ. We also note that $\rho^2 = s^2 + \varsigma^2$ and that $\tan\varepsilon = \tan\theta/\sin(\varphi - \phi)$, where ϕ is the directed phase angle measured from the Sunward direction in the same sense as φ. Using the new coordinate system we rewrite equation (A10) as

$$\varrho_v(s, \varsigma, \varepsilon) = \frac{Q}{\pi\, \upsilon_{gas}}\, \frac{s\cos\phi - \varsigma\cos\varepsilon\sin\phi}{(s^2 + \varsigma^2)^{3/2}}\, e^{-\sqrt{s^2+\varsigma^2}/\rho_p}$$

$$\text{for } s_{\min} \leq s \leq s_{\max}, \qquad (A11)$$

where $s_{\min} = \varsigma\cos\varepsilon\tan\phi$ and $s_{\max} = +\infty$ if the Sunward vector is directed into the Earthward hemisphere ($-90° < \phi < +90°$), and $s_{\min} = -\infty$ and $s_{\max} = \varsigma\cos\varepsilon\tan\phi$ for the anti-Earthward hemisphere ($-180° < \phi < -90°$ and $+90° < \phi < +180°$). If $\phi = -90°$ or $+90°$, $s_{\min} = -\infty$ and $s_{\max} = +\infty$, but the validity of equation (A11) becomes restricted to $-90° \leq \varepsilon \leq +90°$ for $\phi = -90°$, and $-180° \leq \varepsilon \leq -90°$ and $+90° \leq \varepsilon \leq +180°$ for $\phi = +90°$. The function given by equation (A11) can be further integrated along the line of sight to provide the column density profile:

$$\varrho_c(\varsigma, \varepsilon) = \frac{Q}{\pi\, \upsilon_{gas}} \int_{s_{\min}}^{s_{\max}} \frac{s\cos\phi - \varsigma\cos\varepsilon\sin\phi}{(s^2 + \varsigma^2)^{3/2}}\, e^{-\sqrt{s^2+\varsigma^2}/\rho_p}\, ds. \qquad (A12)$$

The obtained density profiles can be compared with the standard density functions for isotropic outgassing (Haser 1957):

$$\varrho_v(\rho) = \frac{Q}{4\pi\, \rho^2\, \upsilon_{gas}}\, e^{-\rho/\rho_p}, \qquad (A13)$$

and

$$\varrho_c(\varsigma) = \frac{Q}{\pi\, \upsilon_{gas}} \int_{-\infty}^{+\infty} \frac{e^{-\sqrt{s^2+\varsigma^2}/\rho_p}}{s^2 + \varsigma^2}\, ds, \qquad (A14)$$

which can be derived in the same way as above, assuming uniform insolation all over the object with a constant $\cos z_\odot = 0.25$ (so

that the total incoming energy be correct). Note that the last function has a simple analytical solution $\varrho_c(\varsigma) = Q/(4\,\varsigma\,\upsilon_{gas})$, when photodissociation is neglected ($\rho_p = \infty$).

A3 Radiative transfer and line profile

To synthesize a line profile, we will solve the radiative transfer equation, and in this way determine the spectral power distribution of the gas environment characterized in the previous section. From now on we assume that the coma is optically thin at the observed frequencies, which simplifies the radiative-transfer equation to

$$\frac{dI(v, s)}{ds} = j(v, s), \qquad (A15)$$

where I [W m^{-2} sr^{-1} Hz^{-1}] is the spectral intensity, j [W\ m^{-3} sr^{-1} Hz^{-1}] is the spectral emissivity, and both are functions of the frequency of electromagnetic radiation v and distance along a given path s. The functions indicate the distribution of spectral power emitted by a given environment into a unit solid angle in a unit frequency interval, the former – from a unit surface element of this environment, and the latter – from a unit volume element. The above equation can be readily integrated to provide the total spectral intensity $I(v)$ generated along the considered path:

$$I(v) = \int_{s_{\min}}^{s_{\max}} j(v, s)\, ds. \qquad (A16)$$

We substitute $j(v, s) = j_{ul}(v, s)$, which is the spectral emissivity of a transition from the upper energy level u to the lower energy level l. It is given by the fundamental physics as

$$j_{ul}(v, s) \equiv \frac{1}{4\pi}\, h v_{ul}\, A_{ul}\, \varrho_v(s)\, f_u(s)\, \psi_{ul}(v, s), \qquad (A17)$$

where $h = 6.626\,068 \times 10^{-34}$ J Hz^{-1} is the Planck constant, v_{ul} [Hz] is the transition frequency, A_{ul} [s^{-1} molec^{-1}] is the Einstein coefficient for spontaneous emission, ϱ_v [molec m^{-3}] is the volume density, f_u is the fraction of molecules in the upper energy level, and ψ_{ul} [Hz^{-1}] is the normalized line profile such that $\int_0^\infty \psi_{ul}(v)\, dv \equiv 1$. For the transitions of CO considered in this work we have $v_{10} = 115.271\,2018$ GHz, $A_{10} = 7.2036 \times 10^{-8}$ s^{-1}, $v_{21} = 230.538\,0000$ GHz, $A_{21} = 6.9106 \times 10^{-7}$ s^{-1}, $v_{32} = 345.795\,9899$ GHz, $A_{32} = 2.4966 \times 10^{-6}$ s^{-1} (CDMS; Müller et al. 2005). From equations (A16) and (A17) we obtain:

$$I_{ul}(v) = \frac{1}{4\pi}\, h v_{ul}\, A_{ul} \int_{s_{\min}}^{s_{\max}} \varrho_v(s)\, f_u(s)\, \psi_{ul}(v, s)\, ds, \qquad (A18)$$

which provides the most general formulation of $I_{ul}(v)$ for line emission in the optically thin regime.

It is customary to replace the spectral intensity as a function of frequency $I(v)$ with the brightness temperature as a function of radial velocity $T_B(v_r)$, which is obtained using the Rayleigh–Jeans and Doppler laws:

$$T_B(v_r) = \frac{c^2}{2k_B v_{ul}^2}\, I(v) = \frac{c^3}{2k_B v_{ul}^3}\, I(v_r)$$

$$= \frac{1}{8\pi}\, \frac{h\,c^3}{k_B}\, \frac{A_{ul}}{v_{ul}^2} \int_{s_{\min}}^{s_{\max}} \varrho_v(s)\, f_u(s)\, \psi_{ul}(v_r, s)\, ds, \qquad (A19)$$

where $c = 2.997\,92458 \times 10^8$ m s^{-1} is the speed of light, and ψ_{ul} [(m/s)$^{-1}$] becomes the normalized line profile per unit radial velocity interval, such that $\int_{-\infty}^{+\infty} \psi_{ul}(v_r)\, dv_r \equiv 1$.

To complete the derivation, we need to provide the three functions, the product of which is integrated along the considered path.

Let us only consider the paths parallel to the line of sight. Using again the cylindrical coordinate system oriented along the line of sight, which we introduced in the previous section, we realize that all three functions generally depend also on the distance component normal to the line of sight ς and its a position angle ε defining the considered path. In this coordinate system, the volume density function $\varrho_v(s, \varsigma, \varepsilon)$ for the considered anisotropic outgassing pattern is given by equation (A11), and the integration limits are defined by the domain of this function (see previous section). For the second function, $\psi(v_r, s, \varsigma, \varepsilon)$, we assume that the line profile generated by a single volume element is entirely controlled by the bulk gas flow velocity and the distribution of thermal velocity, both projected on to the line of sight. We assume for this purpose the Maxwell–Boltzmann velocity distribution for a single direction, which applies to ideal gases close to TE:

$$\psi(v_r) = \sqrt{\frac{\mu}{2\pi k_B T}}\, \mathrm{e}^{-\frac{\mu\,(\mathbf{v}_r - v_r)^2}{2k_B T}}, \tag{A20}$$

where $T = T_{gas}(s, \varsigma, \varepsilon)$ is the gas temperature, and $v_r = v_r(s, \varsigma) = -v_{gas}\, s/\sqrt{s^2 + \varsigma^2}$ is the gas-flow velocity component along the line of sight. Note that v_r is negative for the gas-flow velocity vector directed in the Earthward hemisphere (Doppler blueshift) and positive for the anti-Earthward hemisphere (redshift). The resulting line profile has a Gaussian shape with the width controlled by the gas temperature and the centre controlled by the gas-flow velocity component along the line of sight. Finally, we adopt $f_u(s, \varsigma, \varepsilon)$ for FE, established by the solar radiation field. In FE the energy level population can be calculated by balancing the radiative rates leading to and from a given energy level for a number of levels. The rates are controlled by three fundamental radiative processes: spontaneous emission, forced emission, and absorption. In the considered case of CO, we take into account a set of rotational levels within the first two vibrational levels in the ground electronic state $X^1\Sigma^+$, and calculate the energy level distribution following Crovisier & Le Bourlot (1983) and Chin & Weaver (1984). The level population in FE differs to some extent from the population in TE, established by collisions and consistent with the assumed thermal velocity distribution.

In the final step we calculate the main-beam brightness temperature $T_{mB}(v_r)$, which is the standard calibrated quantity resulting from spectral-line observations at millimetre and submillimetre wavelengths. It is a result of integration of the brightness temperature $T_B(v_r, \varsigma, \varepsilon)$ with the main-beam sensitivity profile $G(\varsigma, \varepsilon)$, normalized by the integrated beam profile:

$$T_{mB}(v_r) = \frac{\int_0^{2\pi} \int_0^\infty T_B(v_r, \varsigma, \varepsilon)\, G(\varsigma, \varepsilon)\, \varsigma\, \mathrm{d}\varsigma\, \mathrm{d}\varepsilon}{\int_0^{2\pi} \int_0^\infty G(\varsigma, \varepsilon)\, \varsigma\, \mathrm{d}\varsigma\, \mathrm{d}\varepsilon}. \tag{A21}$$

The beam profile is commonly approximated by a symmetric Gaussian function $G(\varsigma) = \mathrm{e}^{-\varsigma^2/w^2}$, which can be readily integrated yielding $\int_0^{2\pi}\int_0^\infty \mathrm{e}^{-\varsigma^2/w^2}\varsigma\, \mathrm{d}\varsigma\, \mathrm{d}\varepsilon = \pi w^2$. In this equation, w is a parameter related to the angular FWHM of the beam through $w = \mathrm{FWHM}\,\Delta/(2\sqrt{\ln 2})$, where Δ is the distance from the observer and FWHM is specified in radians. If the beam is pointed at an offset position $(\varsigma_0, \varepsilon_0)$ then the Gaussian beam profile becomes

$$G(\varsigma, \varepsilon) = \mathrm{e}^{-\frac{\varsigma^2 + \varsigma_0^2 - 2\varsigma\varsigma_0 \cos(\varepsilon - \varepsilon_0)}{w^2}}, \tag{A22}$$

which makes it possible to calculate off-centre spectra and which simplifies to the previous form for $\varsigma_0 = 0$. Equation (A21) connects the physical model of the coma with the calibrated spectral line profile measured by a radio telescope and therefore completes our derivation.

This paper has been typeset from a TeX/LaTeX file prepared by the author.